Supplementary Information

Chiral Templating of Self-Assembling Nanostructures

by Circularly Polarized Light

Jihyeon Yeom[1], Bongjun Yeom[2], Henry Chan,[3] Kyle W. Smith[4], Sergio Dominguez-Medina[4], Joong Hwan Bahng[5], Gongpu Zhao[6], Wei-Shun Chang,[4] Sung Jin Chang[7], Andrey Chuvilin[8,9], Dzmitry Melnikau,[8,10] Andrey L. Rogach[11], Peijun Zhang[6], Stephan Link[4], Petr Král,[3,12] Nicholas A. Kotov[1,2,5*]

[1]Department of Macromolecular Science and Engineering, University of Michigan, Ann Arbor, MI 48109, USA;

[2]Department of Chemical Engineering, University of Michigan, Ann Arbor, MI 48109, USA;
[3]Department of Chemistry, University of Illinois at Chicago, Chicago, IL 60607, USA

[4]Department of Chemistry, Rice University, Houston TX 77005, USA

[5]Department of Biomedical Engineering, University of Michigan, Ann Arbor, MI 48109, USA;

[6]University of Pittsburgh School of Medicine, Pittsburgh, PA 15260, USA;

[7]Division of Material Sciences, Korea Basic Science Institute, Daejeon, 305-333, Republic of Korea;

[8]CIC NanoGUNE Consolider, Tolosa Hiribidea 76, Donostia-San Sebastian, 20018, Spain;

[9]Ikerbasque, Basque Foundation for Science, Alameda Urquijo 36-5, 48011, Bilbao, Spain;

[10]Centro de Física de Materiales (MPC, CSIC-UPV/EHU), Po Manuel de Lardizabal 5, Donostia-San Sebastian, 20018, Spain;

[11]Department of Physics and Materials Science and Centre for Functional Photonics (CFP); City University of Hong Kong, 83 Tat Chee Avenue, Kowloon, Hong Kong S. A.R.;

[12]Department of Physics, University of Illinois at Chicago, Chicago, IL 60607, USA

*To whom correspondence should be addressed. E-mail: kotov@umich.edu (N.A.K.)

Keywords: chirality, self-assembly, circularly polarized light, nanoribbon, chiroptical properties

ADDITIONAL METHODS

Experimental Methods:

Synthesis and analysis of twisted nanoribbons: CdTe NPs were synthesized with the reduced amount of thioglycolic acid (TGA) stabilizer. We used the literature procedure (*1*) with the TGA to Cd^{2+} ratio of ~1.1. To induce the self-assembly of CdTe NPs, templating chirality of CPL, the amount of TGA in the dispersion was significantly reduced by precipitation and redispersion of CdTe NPs in purified water at pH = 9. The pH was adjusted by the addition of 0.1 M NaOH, and the precipitation was done by addition of methanol followed by centrifugation for 20 min. The dispersion was placed in a dark room, and then exposed to circularly polarized light. As the NPs were assembled into nanoribbons by illuminated CPL, the orange color was turned to dark green.

The morphology of assembled nanoribbons were analyzed by tapping mode atomic force microscopy (AFM) with NTEGRA Spectra tips (NT-MDT), scanning electron microscopy (SEM, FEI Nova), and transmission electron microscopy (TEM, JEOL 3011) To measure optical activity, the nanoribbons were separated from the solution by gentle centrifugation (bench-top centrifuge, 3000 rpm, 3 min) and redispersion in distilled and deionized water. The CD spectra were obtained by a JASCO J-815 instrument. The Fourier transform infrared spectroscopy (FTIR), energy dispersive spectrometry (EDS, JEM-2200FS, JEOL) and X-ray photoelectron spectra (XPS, Kratos Analytical AXIS Ultra) were used to exam the composition of nanoribbons.

Optical set-up for the CPL induced assembly: The green (543 nm) helium-neon laser with random polarization of emitted photons (Research Electro-Optics, Inc. Boulder, Colorado) was used as a light source. The laser emission was transformed to CPL by directing it through a linear polarizer and a quarter-wave plate. Since the quarter-wave plate is made with a birefringent material, the linearly polarized light turned to CPL by passing through the quarter-wave plate with the 45° transmission angle. By rotating the quarter-wave plate 90° relative to the previous angle, the handedness of CPL is changed.

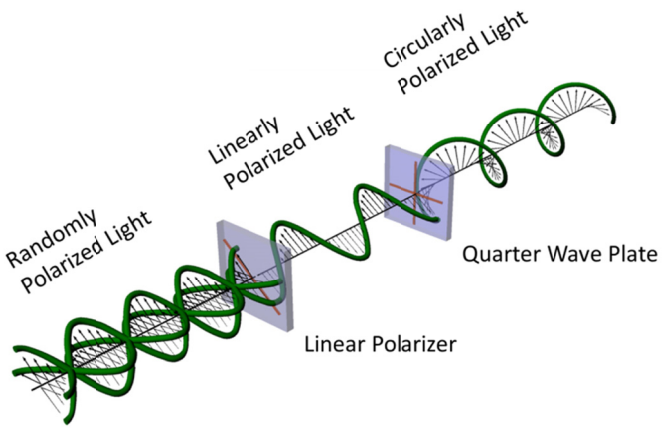

Scheme 1. Schematic illustration of the optical set up for the CPL-templated assembly of NPs.

Chiral separation of racemic CdTe-TGA dispersion with bovine serum albumin (BSA): We chose BSA as a chiral separator because its enantiomeric recognition ability has been studied to separate racemic mixture of amino acids. (*2*) To prevent the interference of residual capping agents in the CdTe NPs dispersion, we centrifuged NPs dispersion, removed supernatant, and then re-dispersed NPs in 50 μM BSA (66.5 kDa) solution. After incubation for 5 h at room temperature in the dark with magnetic stirring, CdTe NPs were separated from BSA by 50 kDa

centrifugal filter (Millipore). The optical activities of obtained CdTe NPs were measured using CD spectrometer (JASCO J-815).

3D TEM tomography: The electron tomography studies at room temperature were carried out on a Tecnai F20 electron microscope (FEI Corporation, Hillsboro, OR.) equipped a Gatan 4K × 4K CCD camera and a field emission gun (FEG) operating at 200 kV. A series of 2D projection images were recorded at a nominal magnification of × 11,500 by tilting the specimen from -75º to 60º for LH nanoribbons and -66º to 75º for RH nanoribbons in increments of 1.5º. Images were recorded at an underfocus value around 7 μm. Colloidal nanogold particles of 15 nm in diameter were used as fiducial markers to aid tracking during data collection and image alignment during reconstruction. A tomography reconstruction software package IMOD (*3*), was used to align the tilt series and calculate three-dimensional tomograms using a weighted back projection algorithm. The surface rendering was generated using the UCSF Chimera software (*4*).

Single nanoribbon scattering, extinction, and CD spectroscopy: Measurements of scattering spectra on single twisted nanoribbons were performed with a homebuilt dark-field microscope. In brief, the unpolarized light from a halogen lamp used as a light source was focused by an oil-immersion dark-field condenser (Zeiss, N.A. = 1.40) and transmitted scattered light was collected by a 50X air-spaced objective (Zeiss, NA = 0.8) and guided to either an avalanche photodiode detector (Micro Photon Device) or a spectrometer equipped with a liquid nitrogen cooled CCD camera (Horiba Jobin Yvon). Nanoribbons were deposited on an indexed microscope coverslip, which was mounted on a XY piezo scanning stage (Physik Instrumente). The scattering images were taken by scanning the sample with the piezo stage across a 50 μm

pinhole located at the first image plane of the microscope and the scattering signal was detected by the avalanche photodiode detector. A LabView interface was designed to synchronize the stage movement and the data acquisition. A typical image was composed of 128 x 128 pixels with an integration time of 5 ms/pixel. Single-nanoribbon spectra were collected by positioning the particle of interested over the pinhole and then guiding the light toward the CCD camera. All measured single-nanoribbon spectra were corrected for the background scattering and normalized by the intensity of the excitation light.

Single-nanoribbon CD measurements were performed when a polarizer followed by a quarter-waveplate were placed before the dark-field condenser. Left-handed and right-handed circular polarization was controlled with the fast axis of the quarter-waveplate set to -45deg and 45deg with respect to the axis of the polarizer, respectively. The CD spectrum was calculated by subtracting the scattering spectrum for right-handed circular polarization from that taken with left-handed circular polarization.

In our previous work, a correction procedure was developed for single particle CD measurements and applied here for any slight deviations from perfectly circular polarization of the incident radiation at the sample based on CD measurements of randomly orientated single gold nanorods. (*5*) In the context of this study they can be considered to be achiral and thus should have no CD signal We find that ellipticity in the polarization of the excitation light gives rise to artifact CD signals of the gold nanorods as a function of their relative orientation with respect to the major/minor axes of elliptically polarized light. Measurement of numerous gold nanorods at different orientations, determined first by taking linearly polarized spectra, allowed us to construct a correction factor for our single particle scattering CD measurements. We

applied this orientation-dependent correction factor to the nanoribbons. To further test the validity of this procedure for the system studied here we collected single particle CD spectra of the same nanoribbon as a function of its orientation by rotating the sample. The results are shown in Figure S13 and the independence of the CD spectra on nanoribbon orientation illustrate that our correction procedure eliminates artifacts in the CD spectra originating from non-perfect circular polarization. It should further be noted that this correction procedure specifically addresses deviations from circular polarized excitation light, while using a condenser to excite the sample ensured that light was incident from all angles, effectively averaging the CD response over all orientation and establishing an important correspondence to ensemble measurements in solution

Single nanoribbon extinction measurements were performed using a microscope setup, in which light from a lamp at normal incidence was focused on the sample using an objective. Comparison between the light intensity collected with and without the nanostructure of interest present in the observation area yielded the extinction. All data analysis was carried out using MatLab software.

Simulation of chiroptical properties: Optical activities of chiral structures were computationally simulated using a COMSOL Multiphysics software package with wave-optics module. Computational models for twisted ribbons used in the simulations were based on the experimental data obtained from SEM, TEM and AFM (Figs. 1 and 2). The model twisted ribbons had a width, thickness, and pitch length of 100 nm, 10 nm, and 300 nm, respectively. Optical constants of CdS were adapted from Ref (*6*).

The *g*-factors obtained for single nanoribbons can be compared to those reported for small organic molecules after plasmon enhancement g = 0.005 (*7-9*), assembled gold NPs on DNA g = 0.02 (*10*), polyaromatic compounds g = 0.05 (*11*), and protein complexes g = 0.06 (*12*).

For simulation of chiroptical properties, the COMSOL models of NPs were created. To simulate random orientation, CD values are calculated from average of directional CDs with light propagating directions of two spherical angles, θ (0 to π) and φ (0 to 2π) with a step of π/6. The environment was water (n=1.33). Characteristic optical constants of CdTe NPs were obtained from Ref (*13*).

CdTe NPs were truncated along three apexes but in different positions to create chiral geometry (Figs. 3G-3I). For an *L*-type nanoscale cluster, four truncated NPs were arranged in space accordingly. The sizes of each NP were scaled as 0.75, 1, 1.1, and 1.2 to reflect the polydispersity of NPs. The L-cluster was mirrored to the plane of x = 0 to obtain an *R*-cluster.

E-DLVO calculations:

Interaction potential (E-DLVO) between nanoparticles

The extended DLVO interaction energies between nanoparticles were approximated by the following expression:

$V_{EDLVO} = V_{VdW} + V_{DL} + V_{DP}$,

where V_{VdW}, V_{DL}, V_{DP} are van der Waals (VdW), double electric layer (DL) , and dipole-dipole (DP) interaction potentials, respectively.

Van der Waals interaction potential

Van der Waals potential approximated as additive contributions of London dispersion forces between CdTe NPs capped with a shell of TGA can be evaluated as follows (*14, 15*):

$$V_{VdW} = V_{VdW,shell} + V_{VdW,core} + V_{VdW,core-shell} + V_{VdW,shell-core} \ ,$$

where

$$V_{VdW,shelll} = \frac{-A_{232}H_{shell}(m,n)}{12} \ : \ m = \frac{x}{2(R_{CdTe}+d)} \ , n = 1$$

$$V_{VdW,core} = \frac{-A_{131}H_{core}(m,n)}{12} \ : \ m = \frac{x+2d}{2R_{CdTe}} \ , \ n = 1$$

$$V_{VdW,core-shell} = \frac{-A_{132}H_{core-shell}(m,n)}{12} \ : \ m = \frac{x+d}{2R_{CdTe}} \ , \ n = \frac{R_{CdTe}+d}{R_{CdTe}}$$

$$V_{VdW,shell-core} = \frac{-A_{132}H_{shell-core}(m,n)}{12} \ : \ m = \frac{x+d}{2(R_{CdTe}+d)} \ , \ n = \frac{R_{CdTe}}{R_{CdTe}+d}$$

The Hamaker function, *H(m,n)*, is given by:

$$H(m,n) = \frac{n}{m^2+mn+n} + \frac{n}{m^2+mn+m+n} + 2\ln\left[\frac{m^2+mn+m}{m^2+mn+m+n}\right],$$

where x is the shortest distance between the TGA-capped CdTe NPs, A_{131} is the Hamaker constant of CdTe interactions in water (4.85 x 10^{-20} J, value of closely CdS NPs (*16, 17*) was used), A_{232} is the Hamaker constant of TGA interactions in water (5 x 10^{-21} J, which

approximates interactions between hydrocarbon chains in water (*18-20*)), A_{132} relates CdTe and TGA in water. and was approximated from the following relation (*18*) :

$$A_{132} = (\sqrt{A_{11}} - \sqrt{A_{33}})(\sqrt{A_{22}} - \sqrt{A_{33}}) \ ,$$

where $A_{11} = 11.4 \times 10^{-20}$J , value of CdS in air (*21*), $A_{22} = 7 \times 10^{-20}$J (*20*), $A_{33} = 3.72 \times 10^{-20}$J (*18*). R_{CdTe} =5 nm is the radius of CdTe NPs, *d*= 0.76nm, is the thickness of the TGA layer around the NPs.(*22*)

Electrostatic potential associated with double electrical layer

The electrostatic interactions between the NPs can be evaluated using the Poisson-Boltzmann formalism as follows (*23-26*):

$$V_{DL} = 4\pi\varepsilon_o\varepsilon_r(R_{CdTe} + d)^2\Gamma^2\left(\frac{k_BT}{e}\right)^2 \frac{\exp(-\kappa x)}{x+2(R_{CdTe}+d)} \ , \text{ where}$$

$$\Gamma = \frac{8*\tanh(\frac{e\psi_{CdTe-TGA}}{4k_BT})}{1+\sqrt{1-\frac{2\kappa(R_{CdTe}+d)+1}{(\kappa(R_{CdTe}+d)+1)^2}\tanh^2(\frac{e\psi_{CdTe-TGA}}{4k_BT})}} \ ,$$

where ε_0 is the permittivity of vacuum, ε_r is the dielectric constant of water and ψ_{CdTe} is the zeta potential of CdTe-TGA(-6mV) NPs . κ, the reciprocal double layer thickness (Debye length), is given by

$$\kappa = \sqrt{\frac{1000N_Ae^2}{\varepsilon_r\varepsilon_0k_BT}\sum_i M_i \times Z_i^2},$$

where e is electric charge (in Coloumbs), N_A is Avogadro's number, M_i and Z_i are the molar concentration and valency of ions, respectively. The practical Debye length of water is taken to be $\kappa^{-1} \approx 100$ nm (*27-29*).

Dipole-Dipole Interactions

Dipole-dipole interaction potential is approximated by the following (*24, 25*):

$$V_{DP} = \frac{-\mu_{CdTe}^2}{2\pi\varepsilon_o\varepsilon_r} * \frac{1}{r(r^2-4R_{CdTe}^2)}, \text{ where}$$

$$r = x + 2d + 2R_{CdTe}$$

Here, μ_{CdTe} , the dipole moment of CdTe NPs, is taken to be 100 D based on the data reported in (*30, 31*).

Interaction between "naked" CdS NPs:

E-DLVO between CdS NPs

Only the interactions between the CdS NP cores are present in this case because the TGA shell was destroyed during the illumination (see Fig. 3 and Figs. S16-S27). Therefore, distance consideration related to the thickness of the stabilizer layer as opposed to the case of CdTe-TGA NPs, is not required.

$$V_{VdW}(CdS, CdS) = -\frac{A_{131}}{6}\left(\frac{2R_{CdS}^2}{2R_{CdS}x + x^2} + \frac{2R_{CdS}^2}{4R_{CdS}^2 + 4R_{CdS}x + x^2} + ln\left[\frac{4R_{CdS}x + x^2}{4R_{CdS}^2 + 4R_{CdS}x + x^2}\right]\right)$$

$$V_{DL} = 4\pi\varepsilon_o\varepsilon_r {R_{CdS}}^2 \Gamma^2 \left(\frac{k_B T}{e}\right)^2 \frac{\exp(-\kappa x)}{x+2R_{CdS}} \ ,$$

where

$$\Gamma = \frac{8*\tanh(\frac{e\psi_{CdS}}{4k_B T})}{1+\sqrt{1-\frac{2\kappa R_{CdS}+1}{(\kappa R_{CdS}+1)^2}\tanh^2(\frac{e\psi_{CdS}}{4k_B T})}}, \qquad \psi_{CdS} = -15\text{mV}$$

$$V_{DP} = \frac{-\mu_{CdS}^2}{2\pi\varepsilon_o\varepsilon_r} * \frac{1}{r(r^2-4R_{CdS}^2)} \ ,$$

where

$r = x + 2R_{CdS}$, $\mu_{CdTe} = \mu_{CdS}$.

Atomistic computer simulations of the assembly of chiral NPs

The modeled NPs have side length of 3.6 nm (10 Cd layers), and they are made of cadmium and sulfur atoms in F43m space group arrangement with a lattice constant of a = 0.582 nm (layer-to-layer distance = 3.16 A). 2, 3, and 4 layers are cut from three of the four vertices to give the NP chirality. Fig. 4A shows a model NP with left and right handedness, respectively. The sulfur atoms are colored based on the number of bonding neighbors and their partial charges are assigned based on that. The partial charges was assigned as 0.4e to cadmium atoms, 0.0655e to sulfur with 1 bonding neighbor (S1), -0.185e to S2, -0.35e to S3, and -0.4e to S4.

The NPs were assembled into a flat layer and the structure was solvated in water. The NPs were subsequently charged by homogeneously distributing the charges to all atoms of the NP. Chloride ions were added to the water to neutralize the NP net charges. We simulated the systems in the NAMD software with CHARMM force field under the condition of periodic boundary, isothermal–isobaric (Gibbs) ensemble at T = 300 K maintained by Langevin dynamics with a damping coefficient of γ_{Lang} = 0.01 ps^{-1}, and long range electrostatic computed using particle mesh Ewald (PME) summation. Furthermore, we added bulk VdW coupling to the NPs (beyond the normal VdW cutoff distance) by adding forces to the center of all NPs. Averaged twist angle of the nanoribbons was calculated from the last ~ 5-10 ns of the simulation trajectory.

ADDITIONAL FIGURES AND COMMENTS

Comment 1: **Self-assembly intermediate stages**. The CdTe NPs aqueous dispersion with a concentration of 0.35 μM was irradiated with RCP or LCP with the intensity of 30 μW, which were lower than the parameters of the previous work, 5 μM and 61 μW respectively (*1*). Contrast to the dog-bone shaped NPs intermediate stages in the Ref. 29, with our experiment conditions demonstrated in this paper, NPs were assembled into twisted nanoribbons individually, not the bundled structures (Figs. 1A and 1B).

Comment 2: After illumination with light for 96 h, some nanoribbons became thinner but the twisted geometry was preserved (Fig. S2). NPs that did not successfully assemble into nanoribbons, agglomerated into randomized aggregation. Thus, the supernatant from nanoribbons dispersion rarely had absorbance signal (Fig. S15). Contrast to the light activated procedure, the NPs dispersion retained its absorbance signal in the dark.

Comment 3: Compared to exposure of 543 nm light, when we used 607 nm wavelength as a light source, the efficiency of chiral selective activation was significantly reduced. The non-activated NPs were dominant around the nanoribbons (Fig. S10). These results indicate that effective absorption of light is important for the efficiency of chiral self-assembly of NPs.

Comment 4: **Phase transition from CdTe to CdS.** The characteristic UV-Vis absorption peak of TGA at 276 nm decreased continuously as we increased the illumination time (Fig. S16). With the analysis of FTIR spectra from original NPs, purified nanoribbons, and supernatant, we found that typical TGA peaks at 3500 cm^{-1}, 1567 cm^{-1}, and 1421 cm^{-1}, respectively, were significantly decreased in nanoribbons compared to the original CdTe NPs (Fig. 3A). A peak from ν_{as}(COO-) of carboxyl moieties was observed in the supernatant, indicating TGA decomposition. XPS spectra of original CdTe NPs and nanoribbons obtained in the S 2p region had peaks at 164.8 eV from thiol groups and 161.6 eV from S in CdS respectively (Fig. S17). In Te 3d region, CdTe NPs show peaks at 572.7 eV and 583.5 eV, corresponding to 3d levels of Te in CdTe (Fig. S18). The nanoribbons revealed XPS peaks at 576.2 eV and 586.5 eV corresponding to TeO_2. They indicated that illumination resulted in (expected) oxidation of Te^{2-} to Te^{4+}.(*1*) Besides XPS, the atomic composition of the nanoribbons was also investigated by energy dispersive spectroscopy (EDS) in TEM. The nanoribbons selected by the dark-field TEM (Fig. S22) were imaged for the presence of Cd, S, and Te. The EDS element maps in Fig. S26 show that the intensity from Cd (green) and S (blue) was significantly higher than that from Te (red). The same conclusion can be reached for line-scanned EDS spectra (Fig. S23). In addition, the absorption peaks of CdTe NPs showed a gradual *blue* shift from 532 nm to 510 nm instead of the typical *red* shift of optical features found in many other NPs assemblies (Fig. S27). The blue shift in our case is associated

with the transition of CdTe to CdS that has wider band gap (2.42 eV) than that of CdTe (1.45 eV).

Comment 4: **CD spectra at various illumination time points.** CD spectra of purified nanoribbons were measured in aqueous dispersions at various illumination time points (Fig. S5). After 12 h of illumination, CD signal appeared at 550 nm. As we increased the illumination time to 28 h, a new peak appeared at 700 nm when the peak at 550 nm was decreased. With more than 36h illumination, the samples revealed distinct chiroptical bands at 490, 590, and 700 nm (Fig. 1F). More importantly, supernatant showed opposite signs to that from nanoribbons.

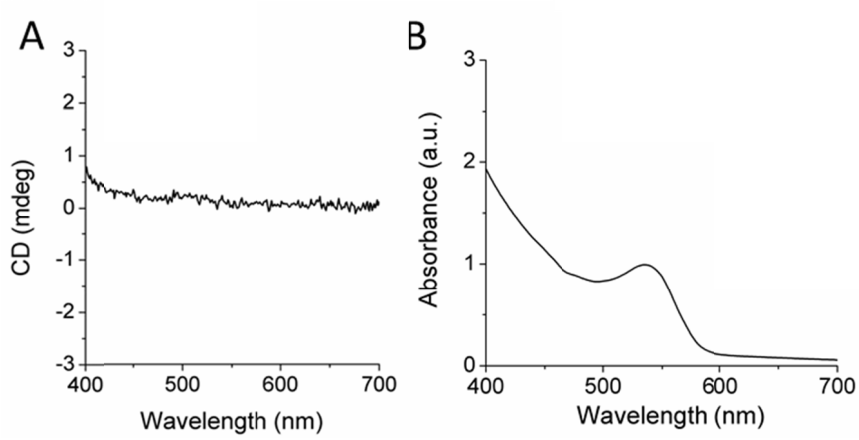

Figure S1. CD (A), and UV-Vis absorption (B) spectra of TGA-stabilized CdTe NPs.

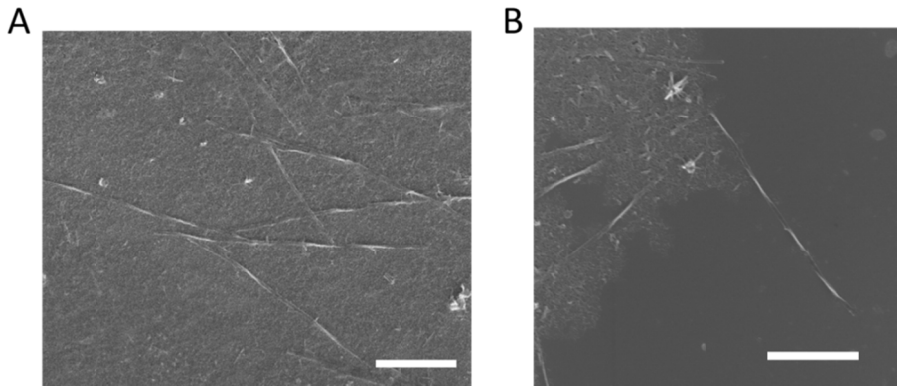

Figure S2. SEM images of nanoribbons after exposure to RCP (A) and LCP (B) light for 96 h (scale bars are 1 um).

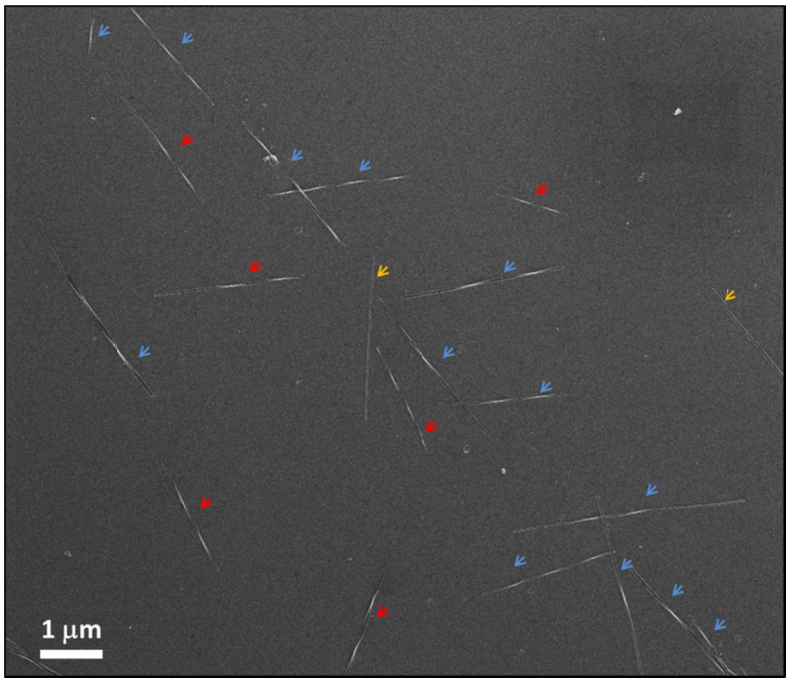

Figure S3. SEM image of nanoribbons after exposure to LCP light for 50 h. Blue, red and yellow arrows indicate LH, RH and non-twisted nanoribbons respectively. With total 21 wires in the image, 61.9 % LH, 28.6 % RH, and 9.5 % non-twisted nanoribbons are observed.

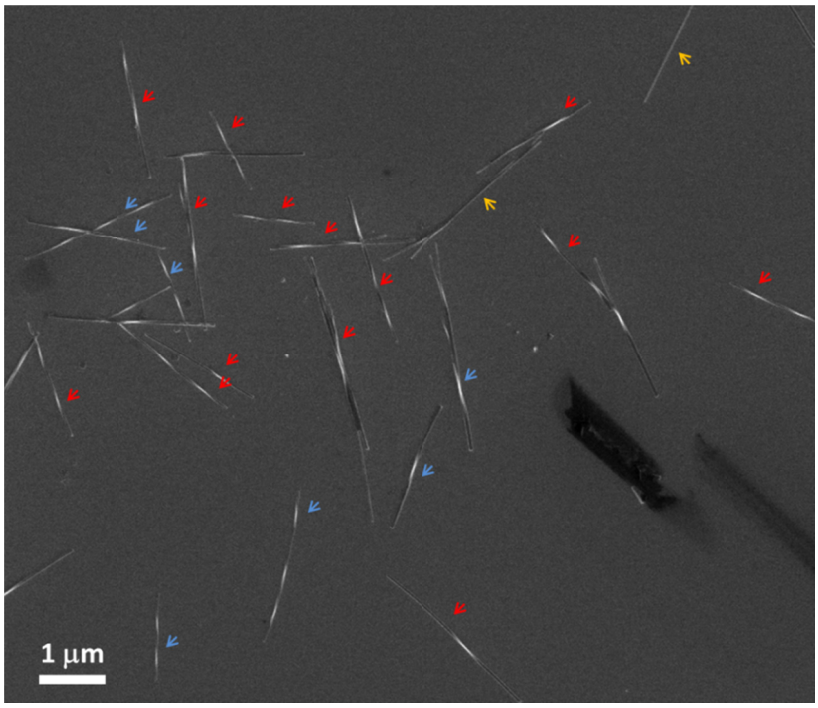

Figure S4. SEM image of nanoribbons after exposure to RCP light for 50 h. Blue, red and yellow arrows indicate LH, RH and non-twisted nanoribbons respectively. With total 23 wires in the image, 30.4 % LH, 60.9 % RH, and 8.7 % non-twisted nanoribbons are observed.

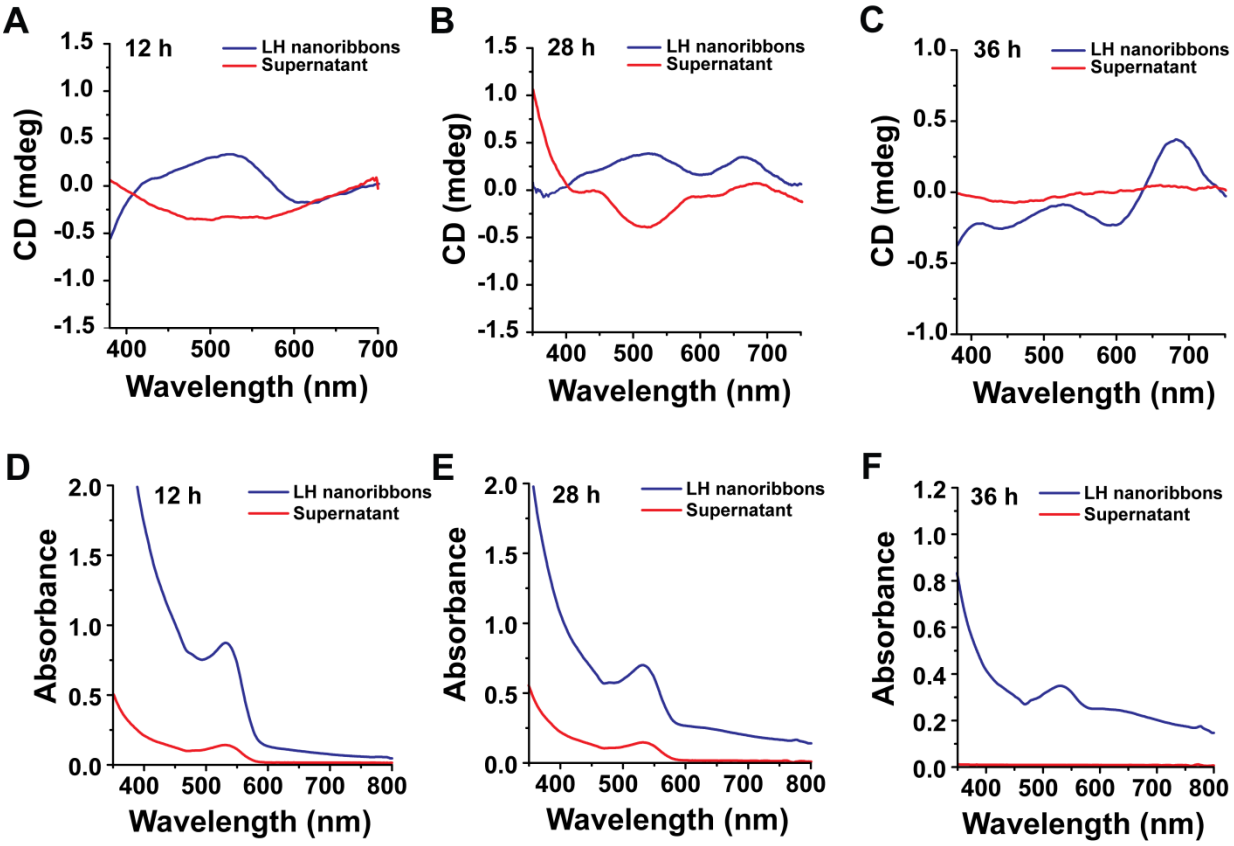

Figure S5. CD (A, B and C) and UV-Vis absorption spectra (D, E, and F) of LH nanoribbons and supernatant after illumination of 12h, 28h, and 36h, respectively.

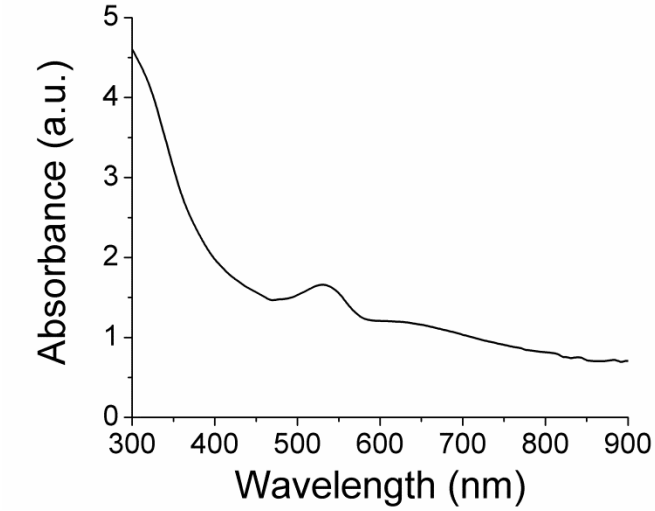

Figure S6. UV-Vis absorption spectra of RH nanoribbons corresponding to Fig. 1F.

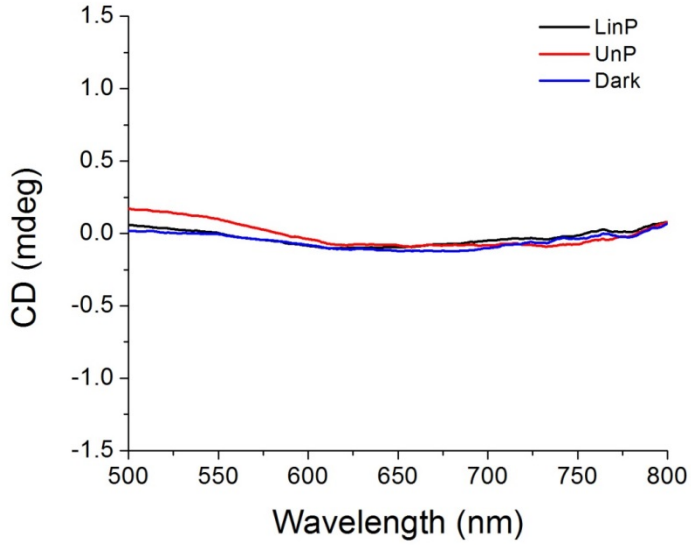

Figure S7. CD spectra of nanoribbons synthesized under UnP, LinP and in the dark.

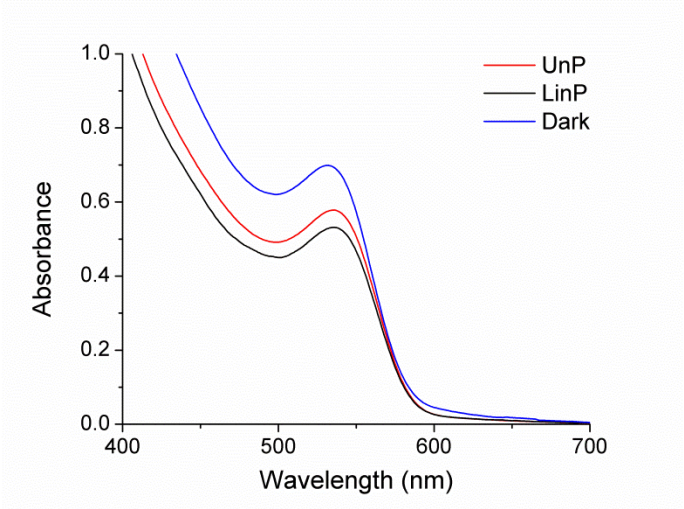

Figure S8. Absorption spectra of nanoribbons synthesized under UnP, LinP and in the dark.

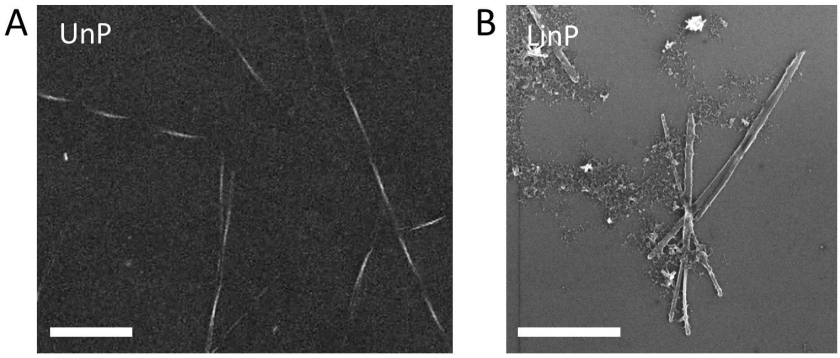

Figure S9. SEM images of nanoribbons self-assembled under UnP (A) and LinP (B). Both scale bars are 1 μm. The population of nanoribbons were significantly lower than NPs.

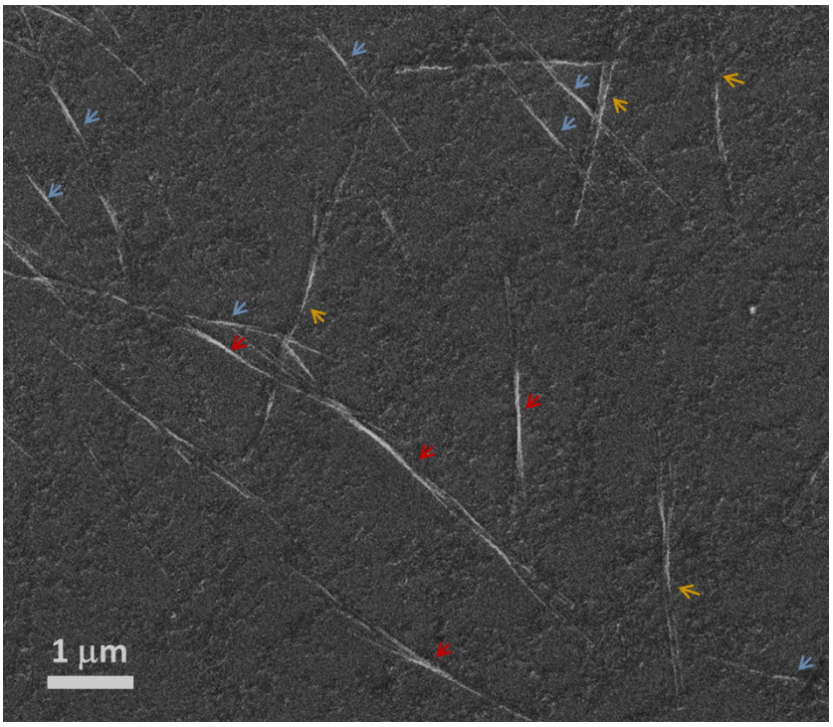

Figure S10. SEM image of nanoribbons after exposure to 603 nm LCP light for 50 h. Blue, red and yellow arrows indicate LH, RH and non-twisted nanoribbons respectively. With total 15 wires in the image, 46.6 % LH, 26.7 % RH, and 26.7 % non-twisted nanoribbons are observed.

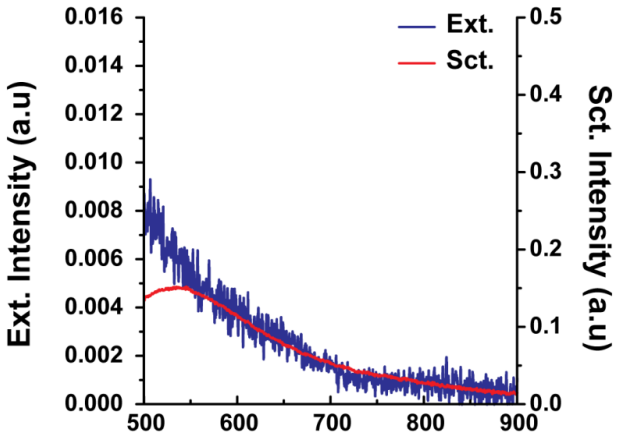

Figure S11. Extinction (blue) and scattering spectra (red) of a single nanoribbon assembled under LCP for 50 h.

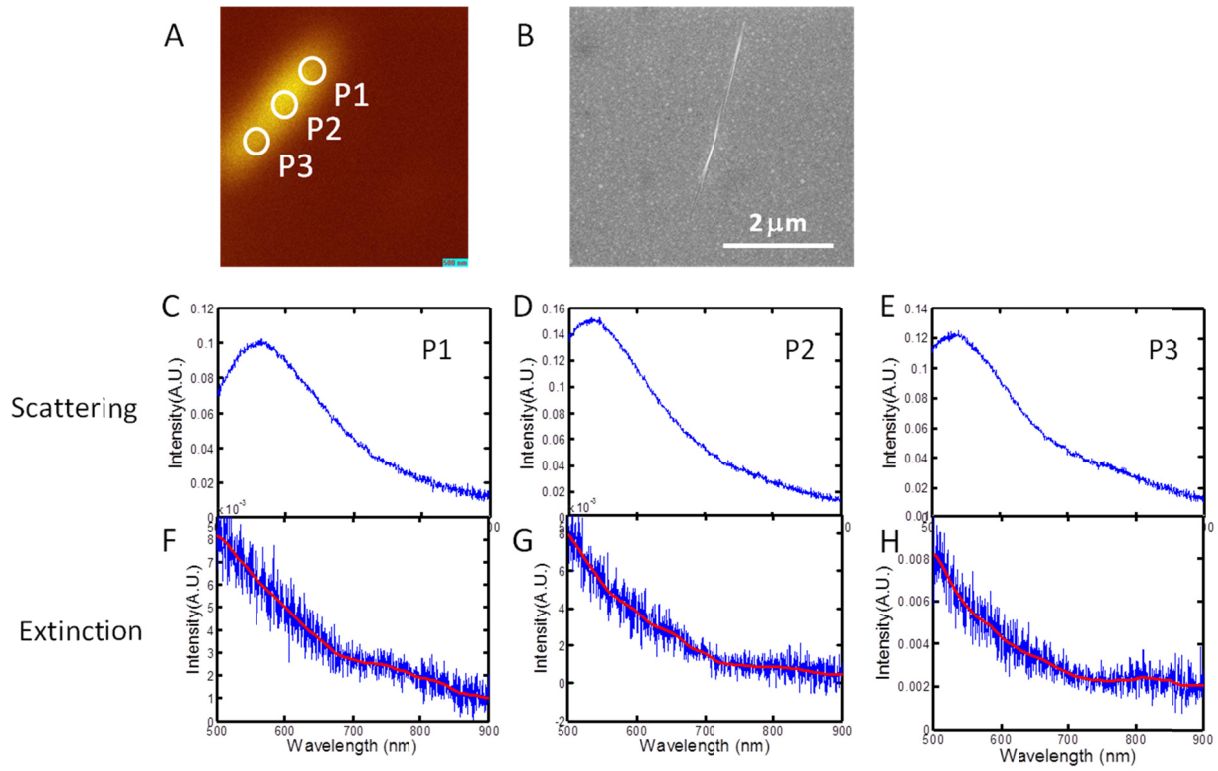

Figure S12. A, Optical image of measured LH nanoribbons synthesized by 50 h illumination of LCP. **B,** SEM image of the corresponding nanoribbon in A. **C, D,** and **E,** Scattering spectra from three different positions of the nanoribbon: P1, P2 and P3 as indicated in A. **F, G,** and **H,** Extinction spectra obtained from P1, P2 and P3.

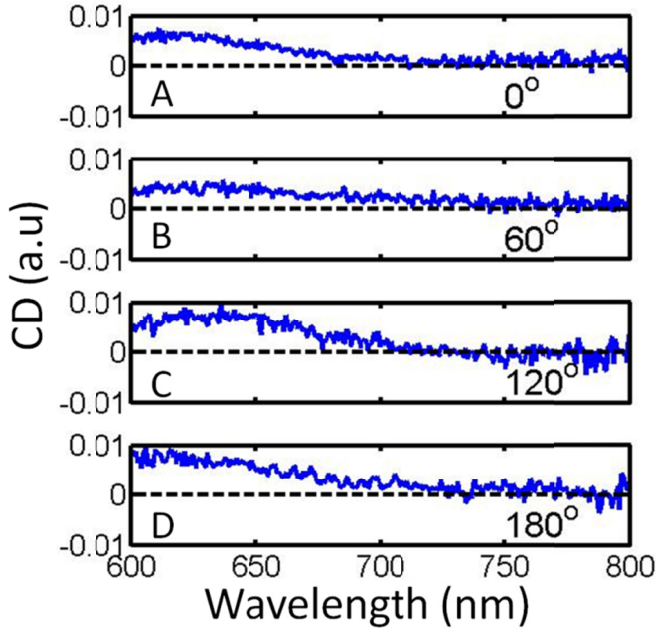

Fig S13. CD spectra of a single nanoribbon measured with the long axis of the nanoribbon orientated at 0° (A), 60° (B), 120° (C), and 180° (D) relative to the lab axis.

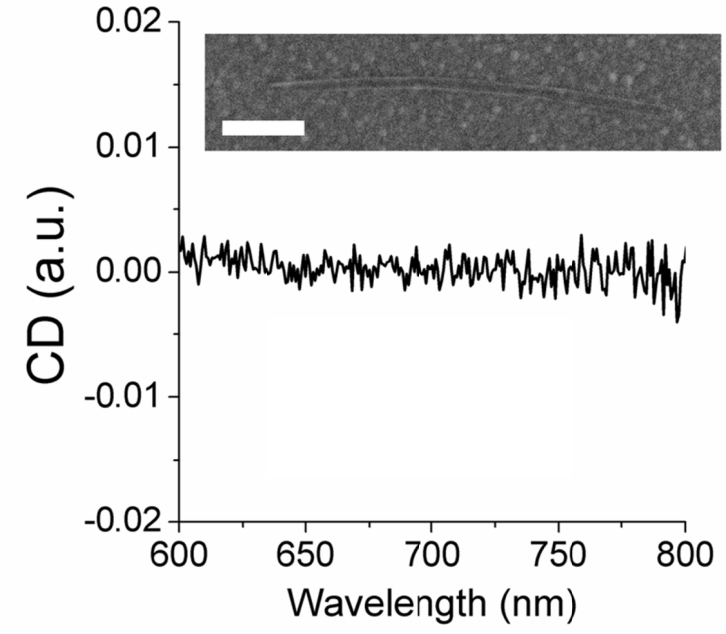

Fig S14. CD spectra of a single non-twisted nanoribbon. Inset: SEM image of the corresponding nanoribbon. Scale bar is 500 nm.

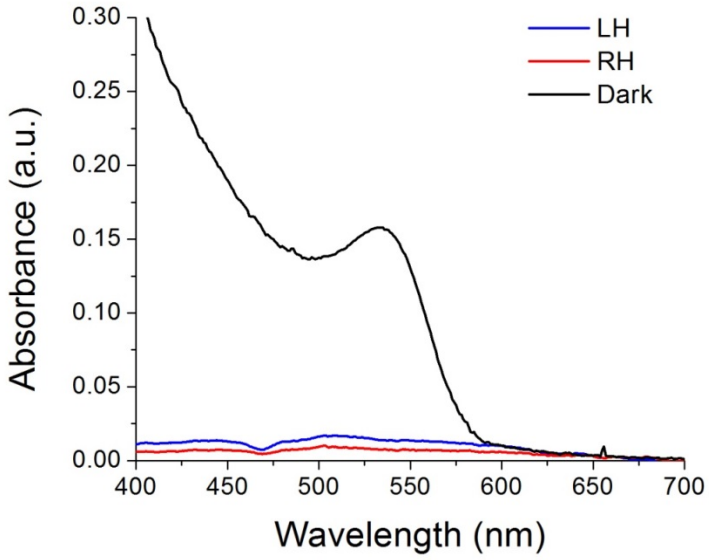

Figure S15. UV-Vis absorption spectra of supernatant separated by centrifugation from nanoribbons obtained with LCP (blue), RCP (red) illumination, or incubation in the dark (black) for 96 h. As shown in SEM images (Fig. S4), NPs present in dispersions aggregate around nanoribbons as a result of centrifugation, so that few NPs remain in the supernatant. Without exposure of light, NPs were well-dispersed in the solution.

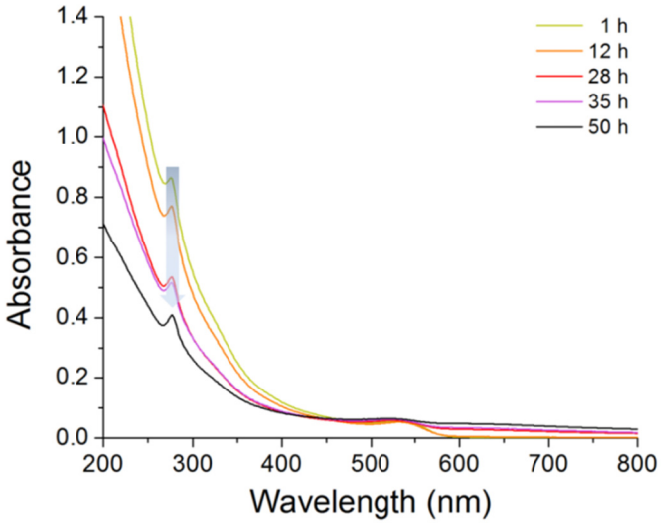

Figure S16. UV-Vis absorption spectra obtained for NP dispersions after illumination with RH light for different lengths of time.

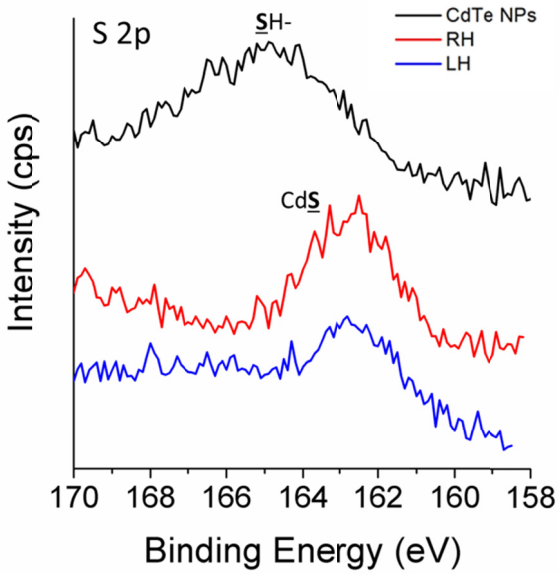

Figure S17. XPS spectra of S 2p region obtained for CdTe NPs, LH, and RH nanoribbons obtained after 50 h of illumination.

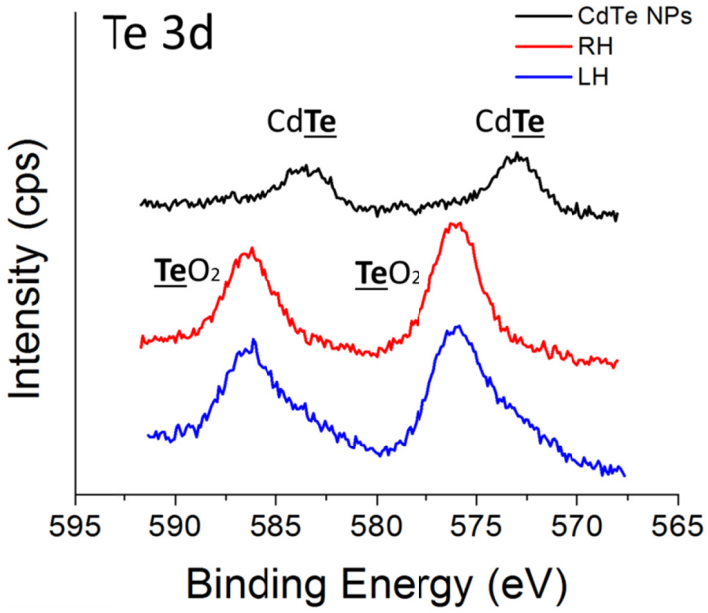

Figure S18. XPS spectra of Te 3d region obtained for CdTe NPs, LH, and RH nanoribbons obtained after 50 h of illumination.

Table S1. Atomic percentage of elements in nanoribbons obtained by EDS (Fig. S22-S24).

Element	Atomic percentage, %
Cd L	51.5
S K	47.3
Te L	1.2

Table S2. Atomic percentage distributions of elements in NPs obtained by EDS (Fig. S25).

Element	Atomic percentage,%
Cd L	49.3
S K	14.5
Te L	36.2

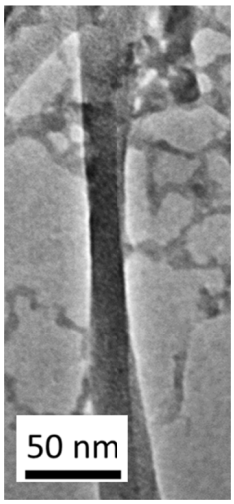

Figure S19. TEM image of LH nanoribbon obtained after 50 h of illumination.

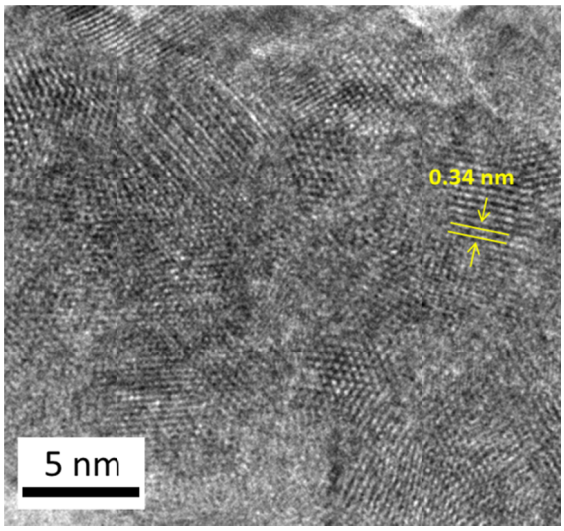

Figure S20. High resolution TEM image of the twist region in LH nanoribbon obtained after 50 h of illumination. The lattice spacing typical for CdS was observed.

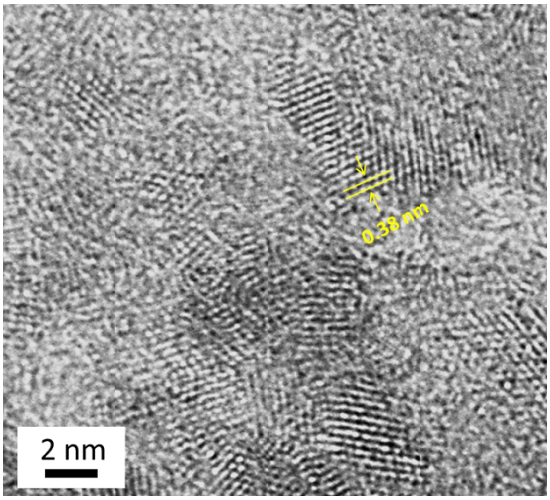

Figure S21. High resolution TEM image of the original CdTe NPs. The lattice spacing typical for CdTe was observed.

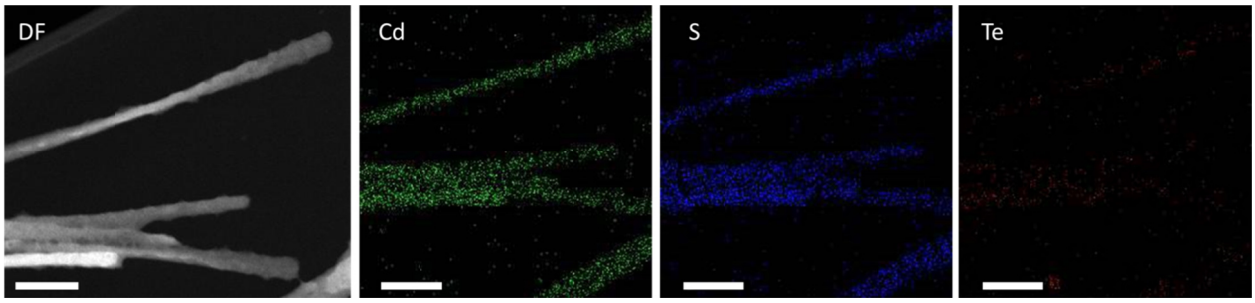

Figure S22. Atomic mapping images of RH nanoribbon obtained after 50 h of illumination time. (All scale bars are 500 nm).

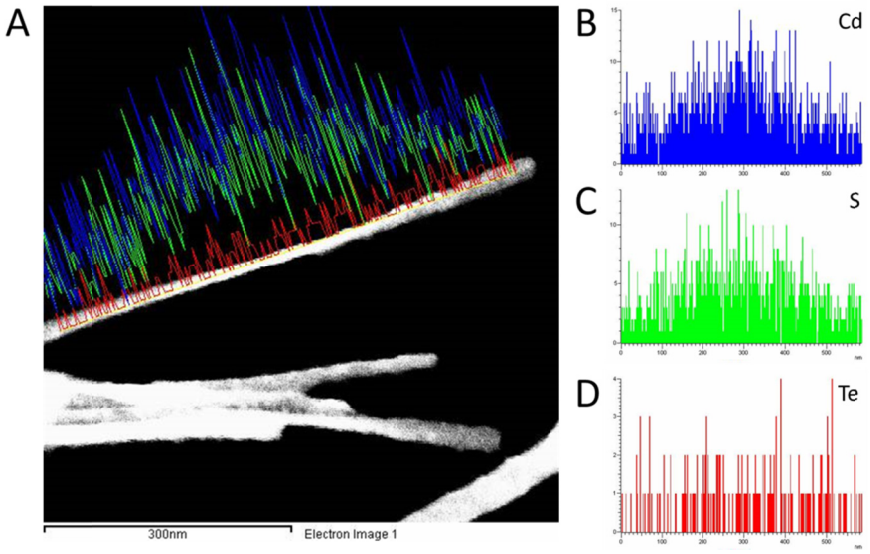

Figure S23. Line-scanned EDS spectra from a single RH nanoribbon obtained after 50 h of illumination.

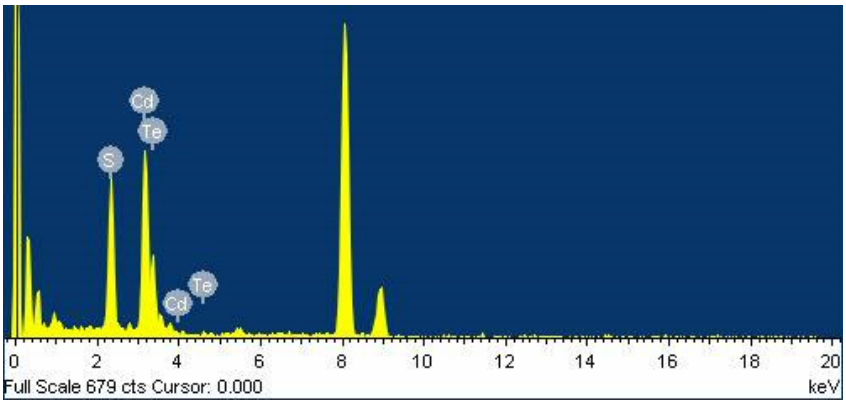

Figure S24. EDS data of RH nanoribbon obtained after 50 h of illumination time.

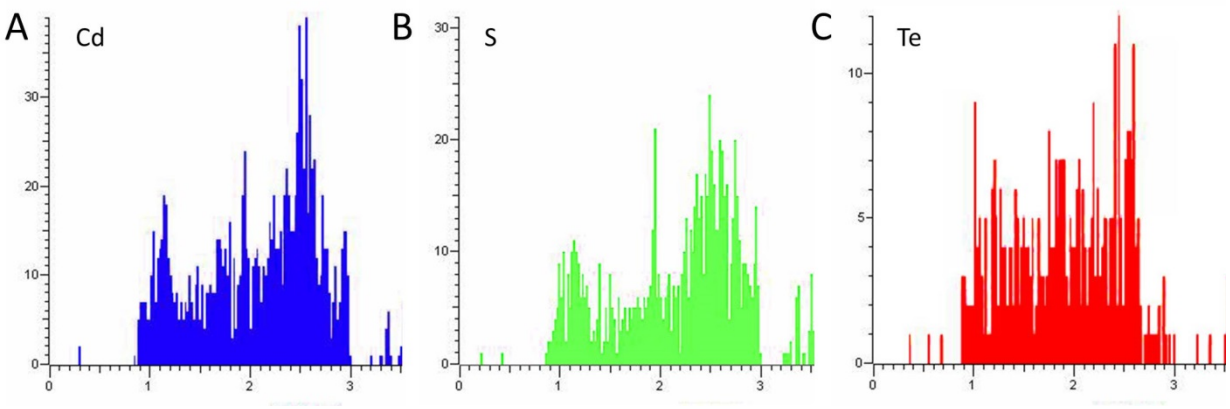

Figure S25. EDS spectra from CdTe NPs.

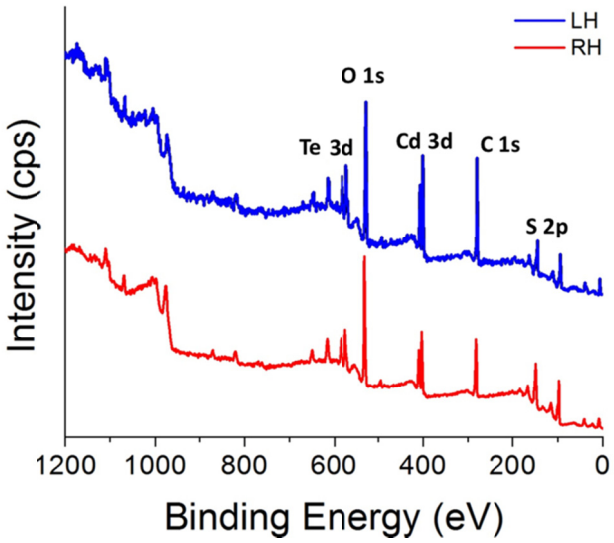

Figure S26. XPS survey spectra of LH and RH nanoribbons obtained after 50 h of illumination.

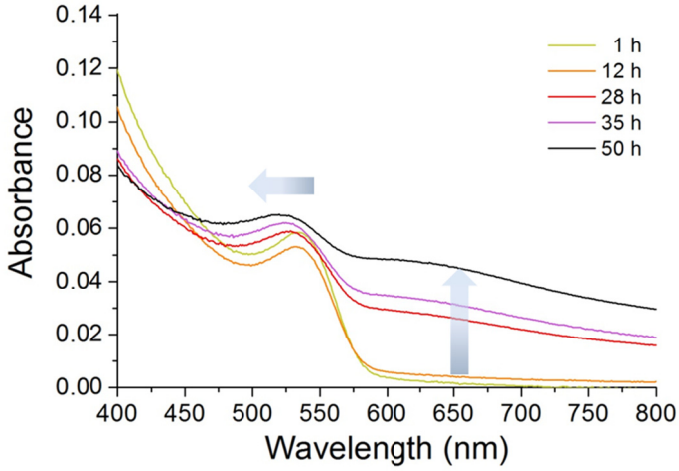

Figure S27. UV-Vis absorption spectra of TGA-stabilized aqueous NP dispersions obtained for various illumination times.

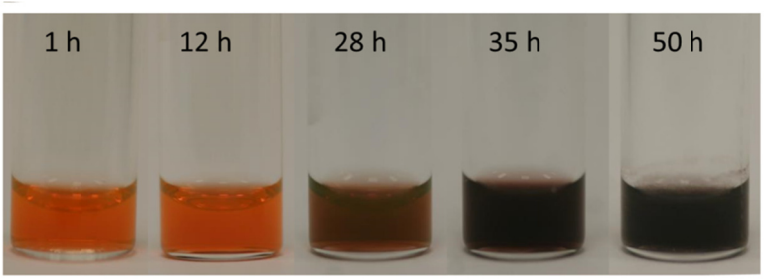

Figure S28. Photographs of the NP dispersions taken for various RCP illumination times.

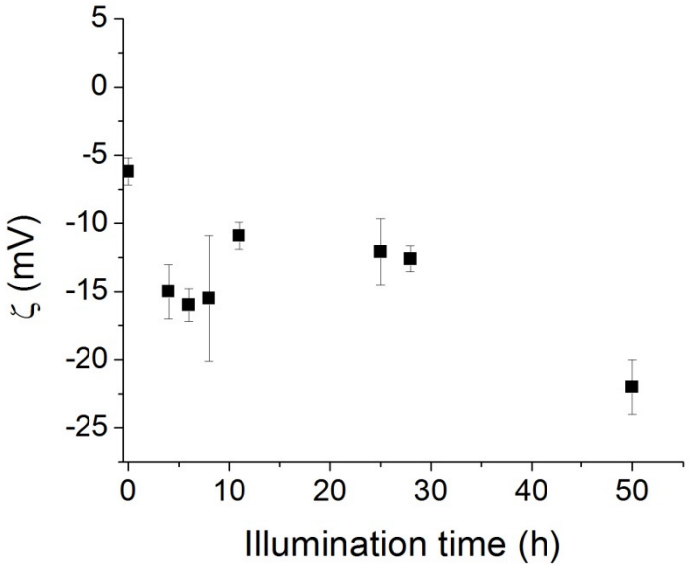

Figure S29. Electrokinetic zeta potential (ζ) for NPs and nanoribbons for various RCP illumination times.

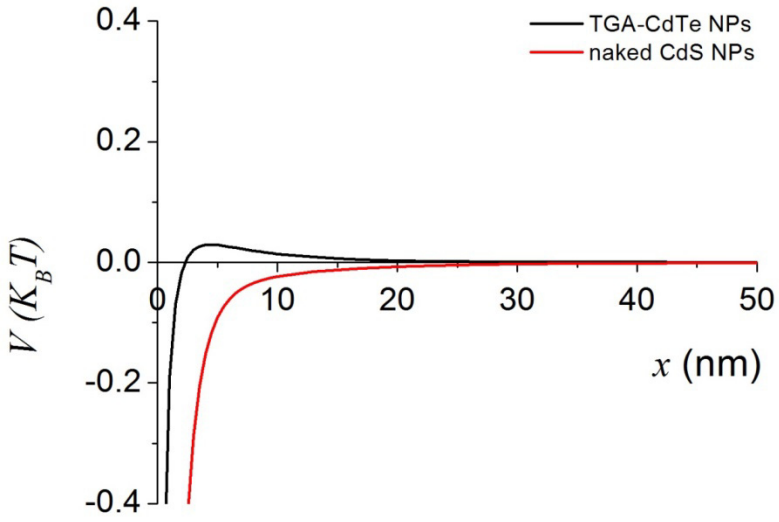

Figure S30. Pair potential calculated based on E-DLVO theory for TGA capped CdTe NPs and surface ligand-free ("naked") CdS NPs.

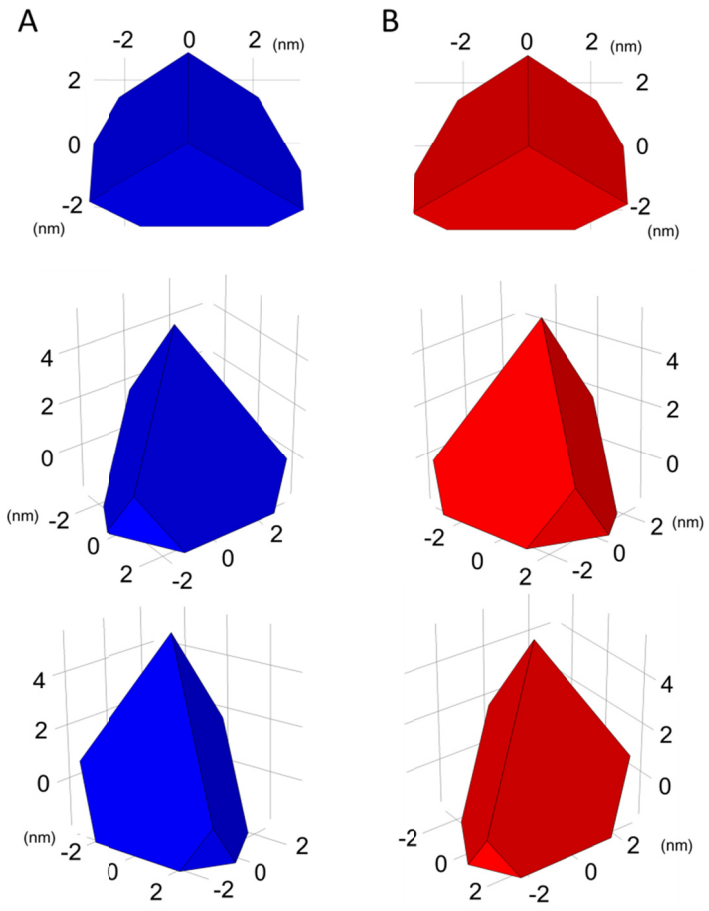

Figure S31. Additional views of COMSOL models of *L*-CdTe NP (A) and *R*-NP (B) used in ME-FEM simulation of CD spectra in Fig. 2D. These images are complementary to those in Fig.2B.

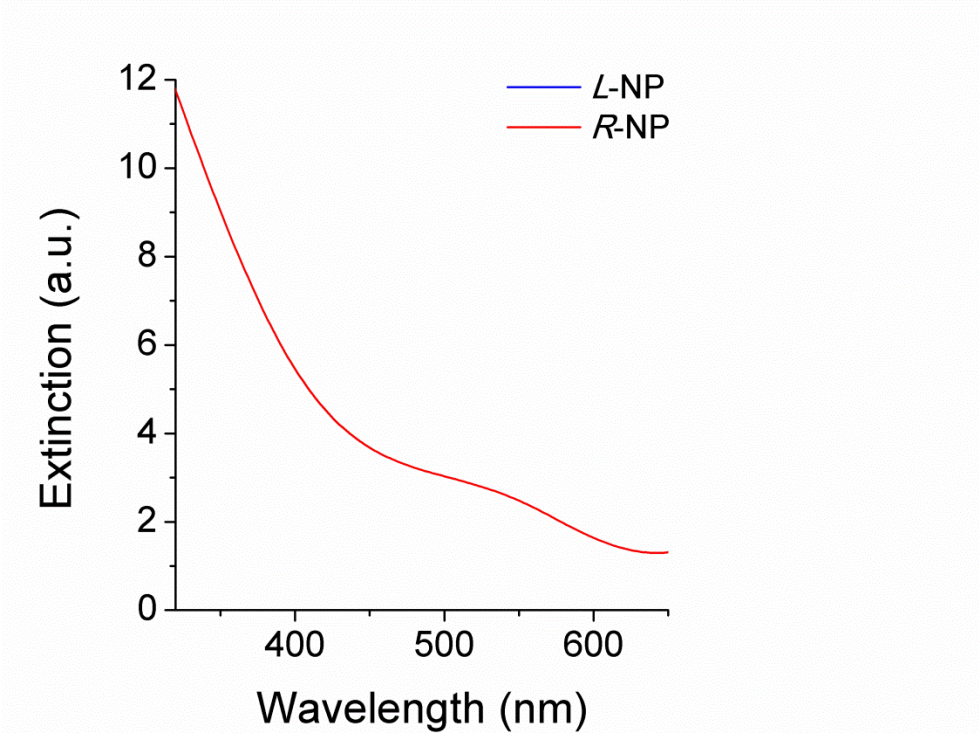

Figure S32. Simulated extinction spectra for *L*/*R*-NPs. The graphs were superimposed.

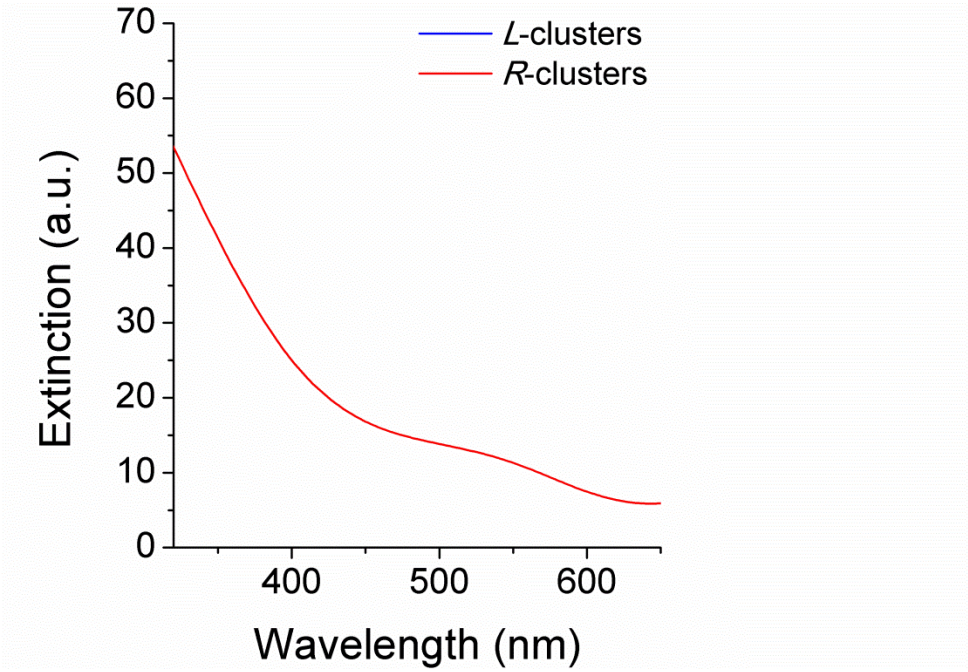

Figure S33. Simulated extinction spectra for*L*/*R*-clusters. The graphs were superimposed.

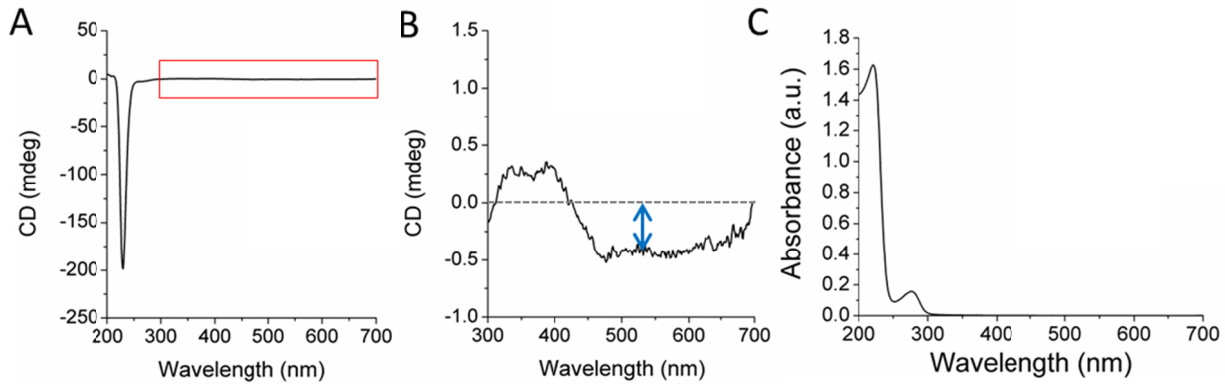

Figure S34. (A) Complete, (B) band-specific CD spectra highlighted in (A) with the red box, and (C) absorbance spectra of BSA .

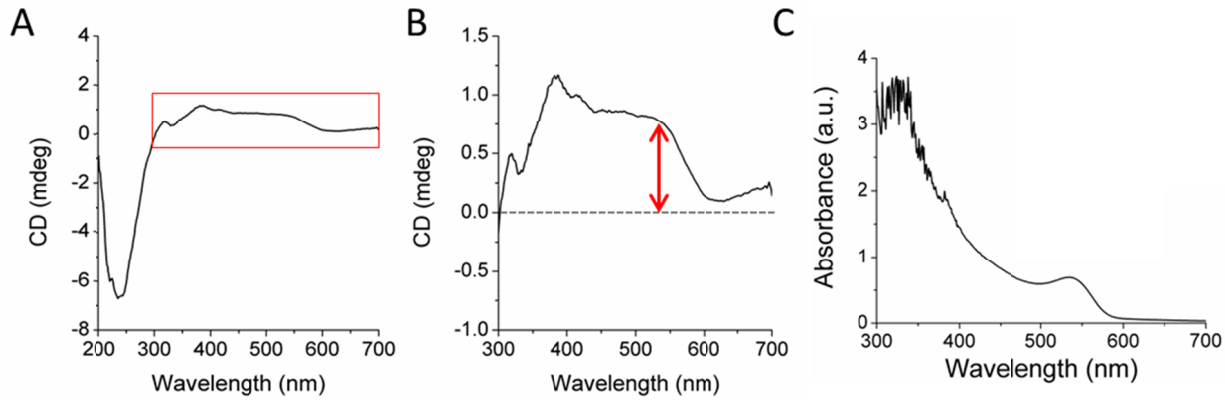

Figure S35. (A) Complete, (B) band-specific CD spectra highlighted in (A) with the red box, and (C) absorbance spectra of CdTe NPs after separation using BSA as an enantioselective agent.

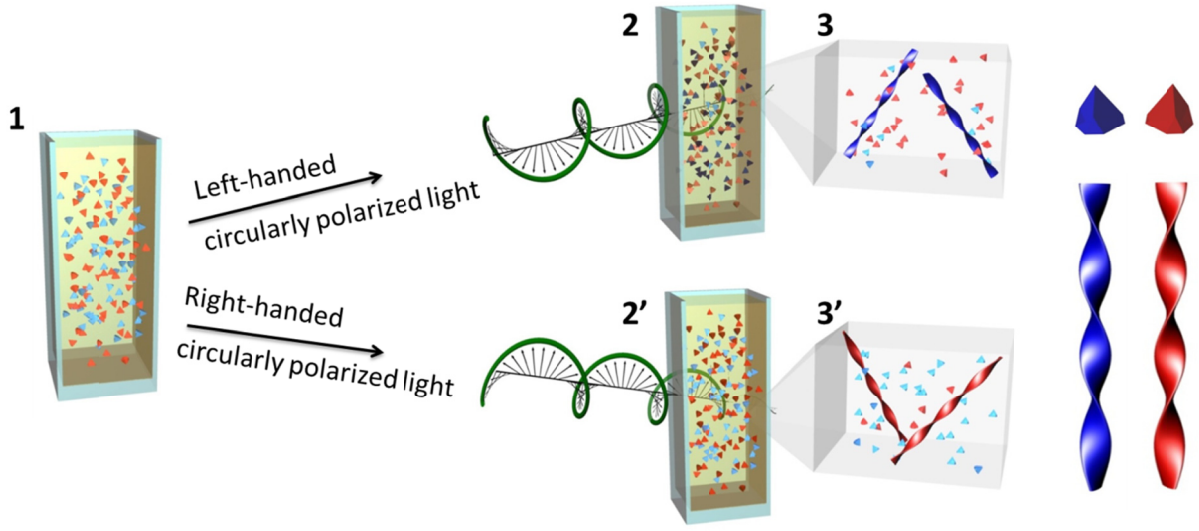

Figure S36. Schematics of the CPL–induced self-assembly process. 1. Racemic mixture of CdTe NPs are prepared. **2.** LCP selectively activates LH NPs. **2'.** RCP activates RH NPs. **3.** The excited LH NPs are self-assembled into LH nanoribbons. **3'.** RH NPs are self-assembled into RH nanoribbons

Comment 5: Light sensitivity of NPs is common. For a few examples other than CdTe, Jin et al.,(*32*) demonstrated controlling Ag NPs shapes using a photoinduced procedure where an aqueous dispersion of spherical Ag NPs were illuminated with a conventional 40W fluorescent light. After 70 h of irradiation, the spherical shapes converted into prisms. Their Ag prims showed unusual optical activities such as Rayleigh light-scatter in the red, and not scattering in the blue, which is common for NPs.

The sizes and polymorphs of NPs are also sensitive to the photoreaction rate.(*33*) Au NPs (3 ~ 30 nm) on TiO_2 were used for photocatalytic hydrogen production from ethanol. The size and polymorph (anatase versus rutile in the case of TiO_2) depended on how the photoreaction rate was controlled.

References for Supplementary Materials

1. S. Srivastava *et al.*, *Science* **327**, 1355 (2010).
2. Wang, Y. Y. *et al. J. Mater. Chem. B* **1**, 5028-5035, (2013).
3. J. R. Kremer, D. N. Mastronarde, J. R. McIntosh, *J. Struct. Biol.* **116**, 71 (1996).
4. E. F. Pettersen *et al.*, *J. Comput. Chem.* **25**, 1605 (2004).
5. Ma, W. et al. Chiral plasmonics of self-assembled nanorod dimers. *Sci. Rep.* **3**, 1934 (2013).
6. E. K. a. S. G. Tomlin, *J. Phys. D: Appl. Phys.* **8**, 581 (1975).
7. A. O. Govorov, Z. Y. Fan, P. Hernandez, J. M. Slocik, R. R. Naik, *Nano Lett.* **10**, 1374 (2010).
8. J. George, K. G. Thomas, *J. Am. Chem. Soc.* **132**, 2502 (2010).
9. A. J. Mastroianni, S. A. Claridge, A. P. Alivisatos, *J. Am. Chem. Soc.* **131**, 8455 (2009).
10. A. Kuzyk *et al.*, *Nature* **483**, 311 (2012).
11. R. S. Walters *et al.*, *J. Am. Chem. Soc.* **130**, 16435 (2008).
12. R. M. Pearlstein, R. C. Davis, S. L. Ditson, *P. Natl. Acad. Sci-Biol.* **79**, 400 (1982).
13. S. Chandra, S. T. Sundari, G. Raghavan, A. K. Tyagi, *J. Phys. D Appl. Phys.* **36**, 2121 (2003)
14. B. Vincent, *J. Colloid Interface Sci.* **42**, 270 (1973).
15. S. H. Ebaadi, *Colloids Surf.* **2**, 155 (1981).
16. I. D. Morrison, *Colloidal dispersions : suspensions, emulsions, and foams*. S. Ross, Ed., (Wiley-Interscience, New York :, 2002).
17. A. Y. Sinyagin, A. Belov, Z. N. Tang, N. A. Kotov, *J. Phys. Chem. B* **110**, 7500 (2006).
18. J. N. Israelachvili, *Intermolecular and surface forces*. (Academic Press, Burlington, MA, ed. 3rd, 2011), 674 p.
19. C. Stubenrauch, O. J. Rojas, J. Schlarmann, P. M. Claesson, *Langmuir* **20**, 4977 (2004).
20. T. Ederth, *Langmuir* **17**, 3329 (2001).
21. L. Bergstrom, *Adv. Colloid. Interfac.* **70**, 125 (1997).
22. T. Mizuno, A. Namiki, S. Tsuzuki, *IEEE T Semiconduct M* **22**, 452 (2009).
23. T. Kim, K. Lee, M. S. Gong, S. W. Joo, *Langmuir* **21**, 9524 (2005).
24. H. Zhang, D. Y. Wang, . *Angew. Chem. Int. Ed.* **47**, 3984 (2008).

25. H. Zhang *et al.*, *J. Phys. Chem. C* **112**, 1885 (2008).
26. J. Gregory, *J. Colloid Interface Sci.* **51**, 44 (1975).
27. H. C. Chang, G. Yossifon, E. A. Demekhin, *Annu. Rev. Fluid. Mech.* **44**, 401 (2012).
28. D. Kim, J. D. Posner, J. G. Santiago, *Sensor. Actuat. A: Phys.* **141**, 201 (2008).
29. C. M. Wang, L. Wang, X. R. Zhu, Y. G. Wang, J. M. Xue, *Lab. Chip* **12**, 1710 (2012).
30. S. Shanbhag, N. A. Kotov, *J. Phys. Chem. B* **110**, 12211 (2006).
31. Z. L. Zhang, Z. Y. Tang, N. A. Kotov, S. C. Glotzer, *Nano Lett.* **7**, 1670 (2007).
32. R. C. Jin *et al.*, *Science* **294**, 1901 (2001).
33. M. Murdoch *et al.*, *Nat. Chem.* **3**, 489 (2011).